



RESEARCH ARTICLE

10.1002/2015WR017626

Geomorphological control on variably saturated hillslope hydrology and slope instability

Formetta Giuseppe¹, Silvia Simoni², Jonathan W. Godt³, Ning Lu¹, and Riccardo Rigon⁴

¹Department of Civil & Environmental Engineering, Colorado School of Mines, Golden Colorado, USA, ²Mountain-eering Srl, Bolzano, Italy, ³U.S. Geological Survey, Golden Colorado, USA, ⁴Department of Civil and Environmental Engineering, University of Trento, Italy

Key Points:

- Quantify the impact of topography on saturated-unsaturated hillslope hydrology and slope-stability
- Morphology impact on transient hydrology is not relevant at local but important at catchment scale
- Percentage of unstable areas was 1.3 for planar, 21 for convex, and 33 for convergent morphology

Supporting Information:

- Supporting Information S1

Correspondence to:

G. Formetta,
giuseppe.formetta@unical.it

Citation:

Giuseppe, F., S. Simoni, J. W. Godt, N. Lu, and R. Rigon (2016), Geomorphological control on variably saturated hillslope hydrology and slope instability, *Water Resour. Res.*, 52, 4590–4607, doi:10.1002/2015WR017626.

Received 3 JUN 2015

Accepted 13 MAY 2016

Accepted article online 19 MAY 2016

Published online 18 JUN 2016

Abstract In steep topography, the processes governing variably saturated subsurface hydrologic response and the interparticle stresses leading to shallow landslide initiation are physically linked. However, these processes are usually analyzed separately. Here, we take a combined approach, simultaneously analyzing the influence of topography on both hillslope hydrology and the effective stress fields within the hillslope itself. Clearly, runoff and saturated groundwater flow are dominated by gravity and, ultimately, by topography. Less clear is how landscape morphology influences flows in the vadose zone, where transient fluxes are usually taken to be vertical. We aim to assess and quantify the impact of topography on both saturated and unsaturated hillslope hydrology and its effects on shallow slope stability. Three real hillslope morphologies (concave, convex, and planar) are analyzed using a 3-D, physically based, distributed model coupled with a module for computation of the probability of failure, based on the infinite slope assumption. The results of the analyses, which included parameter uncertainty analysis of the results themselves, show that convex and planar slopes are more stable than concave slopes. Specifically, under the same initial, boundary, and infiltration conditions, the percentage of unstable areas ranges from 1.3% for the planar hillslope, 21% for convex, to a maximum value of 33% for the concave morphology. The results are supported by a sensitivity analysis carried out to examine the effect of initial conditions and rainfall intensity.

1. Introduction

Shallow landslides often occur in steep terrains in response to intense or prolonged rainfall. The local curvature of the ground surface has an influence on landslide-related factors, such as steady state hydrology, erosion, sediment transport, and spatial variation of soil thickness [e.g., *Heimsath et al.*, 1997; *Dietrich et al.*, 2003; *Dietrich and Montgomery*, 1994]. To quantify the impact of topography on hillslope stability, one must first identify the processes directly affected by topography and then understand the effects of these on hillslope stability. In the short-term, topographic influence on landforming processes can be either time-dependent or time-independent. On the one hand, up to the landslide triggering point, topography, spatial variations of soil depth, and material properties are essentially time-independent (of course, the stress field is influenced by transient infiltrations and redistributions). On the other hand, during the post failure phase, all of these aspects are time-dependent. In this paper, however, we are interested in the prefailure stages.

Topography mainly affects slope stability through two main processes: transient hillslope hydrology and sediment transport. Transient hydrology, described by the *Richards* [1931] equation, determines soil moisture changes and related variations in pore water pressure. Sediment transport and erosion determine soil thickness and the amount of sediment available for potential failure. The effect of topography on hydrology has been largely investigated with respect to saturated, subsurface flows. In these cases, topographically driven flows have been shown to generate spatial patterns of soil moisture and pore pressure distributions that play a significant role in shallow landslide triggering [*Dietrich et al.*, 1986; *D'Odorico and Rigon*, 2003]. Clearly, runoff and saturated groundwater flows are driven by gravity and, ultimately, by topography. Understanding whether the landscape morphology has a bearing on subsurface flows in the vadose zone, however, is less intuitive. To this end, *Philip* [1991b] carried out an infiltration analysis on a homogeneous, isotropic, planar slope. Having defined the *downslope* direction as slope parallel, he found that infiltration always generates a downslope subsurface flux component due to gravity. This component is time-dependent, being proportional to $t^{1/2}$ in the short-term and to t in the long. Furthermore, *Philip* [1991a,

1991c] shows that the results found for a planar slope can be extended to convex and concave slopes, provided that the radius of curvature of the terrain surface is small compared to the characteristic infiltration length (about 10 times smaller). According to his work, perturbation effects generated by divergence/convergence on unsaturated subsurface flows are unimportant for usual hillslope topography.

A significant contribution to the understanding of infiltration in partially saturated soils was given by *Iverson* [2000]. He showed that, in the short-term, transient fluxes have a prevalent vertical component for points where $\epsilon = H/\sqrt{A} \ll 1$, (H is the vertical soil depth and A is the upslope contributing area) [*Iverson*, 2000]. However, landslides and debris flows often occur as a consequence of complex interactions between vertical infiltrations and preexisting soil moisture patterns, the latter resulting from catchment-scale subsurface flows and geomorphological features in addition to variable rainfall inputs [*D'Odorico and Rigon*, 2003].

A debate arose regarding the actual existence of the downslope-upslope flow components. *Lu et al.* [2011] showed that within a homogeneous and isotropic hillslope, under time-varying rainfall conditions, vertical downslope, and upslope lateral flows can occur concurrently in different points. In particular, unsaturated, downslope, lateral flow occurs if the point is in a "drying" state ($\frac{\partial \theta}{\partial t} < 0$), while unsaturated, upslope, lateral flow occurs if the point is in a "wetting" state ($\frac{\partial \theta}{\partial t} > 0$).

In partially saturated soils, an increase in moisture content due to rainfall infiltration and the consequent decrease (absolute value) in pore water pressures reduce interparticle stresses. However, although transient infiltration and reduction in soil stress are strictly connected, their effects are often analyzed separately in stability analyses, and usually by assuming a steady state hydrological framework. Examples of physically based models within this context are SHALlow STABILITY analysis (SHALSTAB) [*Dietrich and Montgomery*, 1994], dSLAM [*Wu and Sidle*, 1995], and Stability INDEX MAPping (SINMAP) [*Pack et al.*, 1998; *Lanni et al.*, 2012]. These models couple a simple steady state or quasi-dynamic hydrology with an infinite-slope analysis for the computation of the Factor of Safety (or stability index), defined as the ratio between stabilizing and destabilizing forces [*Taylor*, 1948]. Analyses carried out with models based on the steady state hydrology approach do not account for the effects of transient hydrology. The distributed model TRIGRS [*Baum et al.*, 2010], which uses one-dimensional, analytic, rainfall infiltration models for computing Factors of Safety, represents an advance in this direction. Other examples of models based on the *Richards* equation approximation, and thus capable of taking account of the transient, are presented in *Capparelli and Versace* [2011], *Lepore et al.* [2013], and *Tsai and Yang* [2006].

There are many studies [e.g., *BeVilleville et al.*, 2010; *Mirus et al.*, 2007; *Simoni et al.*, 2008] that have combined two-dimensional or three-dimensional, variably saturated, flow models with slope stability models. *Shao et al.* [2015] coupled a two-dimensional, variably saturated hydrological model with a model for the computation of the local factor of safety to investigate the influence of preferential flow on slope stability. *Ebel et al.* [2010] investigates the effects of the hysteretic nature of the soil-water retention curve on slope stability by coupling a three-dimensional, variably saturated, flow model with a one-dimensional slope stability model.

The effects of topographic curvature on landslide potential are qualitatively known and some applications using empirical, landslide-susceptibility models have been presented [e.g., *Dai and Lee*, 2002; *Carrara et al.*, 2003; *Dahal et al.*, 2008]. However, to our knowledge, these effects have not been quantitatively assessed with 3-D hydrological models.

This paper aims to investigate whether short-term water fluxes are affected by topography and, if so, to what extent these effects influence slope stability at the catchment scale. We analyzed three real slope morphologies (concave, convex, and planar) using the 3-D, physically based, distributed hydrological model GEOTop [*Rigon et al.*, 2006; *Simoni*, 2007; *Endrizzi et al.*, 2014] combined with a module to compute the probability of failure, based on an infinite slope analysis. GEOTop computes water and energy balances dynamically and provides maps of soil moisture and pressure head at user-defined time steps. The stability module, FS, works in concert with GEOTop, carrying out stability analyses based on computed pressure heads and moisture contents. Finally, the probability of failure is computed using the First Order Second Moment method [*Dai and Lee*, 2002; *Baecher and Christian*, 2005].

Results are given for each location and each time step in terms of: pressure head; water content; suction stress; and probability of failure. The relationships between slope and pressure head, water content, and

probability of failure, respectively, have been reported to highlight the influence of topography on instability. For the examples investigated here, it was seen that convex and planar slopes are generally more stable than concave ones.

2. Analysis of the Physical Processes

2.1. Transient Hillslope Hydrology

Rainfall infiltration, and the consequent changes in pore-water pressure, control shallow landslide initiation in the short-term. Specifically, there are four rainfall attributes that, combined with soil hydraulic properties, strongly affect landslide triggering. These are: total amount of rainfall; antecedent storm precipitation; storm duration; and short-term rainfall intensity [Lu and Godt, 2013]. These factors have a direct influence on pore-pressure generation. Indeed, in analyzing the temporal variations in slope stability, one examines the role of pore-water pressure on the stress state of the soil. The Richards [1931] equation describes three-dimensional infiltration and water redistribution processes in variably saturated porous media, and transient processes taking place in unsaturated soil in the shallow subsurface where rainfall infiltration occurs. The Richards equation combines Darcy's law (for a general theory of unsaturated-saturated flow in porous media see Bear [1972]) and the principle of mass conservation for an incompressible fluid;

$$\nabla[\bar{K}(\theta) \cdot \vec{\nabla}(\psi - z)] = \frac{\partial \theta}{\partial t} + S \quad (1)$$

where $\bar{K}(\theta)$ is a generic 3×3 tensor describing the hydraulic conductivity [L/T], θ is the volumetric water content [L^3/L^3], ψ is the pressure head or water potential [L], z is the vertical coordinate, positive downward [L], t is time, and S represents the sink term describing the specific water volumetric losses (root uptake, evapotranspiration, etc.) [T^{-1}]. Transient approaches to modeling slope stability in response to rainfall infiltration typically try to solve this equation. However, there are difficulties in solving the Richards equation, which hinges upon its strong nonlinearity. The coefficients of the partial differential equation, that is to say the components of the hydraulic conductivity $\bar{K}(\theta)$, depend on the pore water pressure or moisture content. However, $\bar{K}(\theta)$ can vary over several orders of magnitude for small changes in water content or pressure head. Although analytical solutions have been found for one-dimensional forms of the Richards equation under particular boundary conditions [Parlange, 1972; Philip, 1991b; Srivastava and Yeh, 1991; Iversen, 2000], a general, analytical closure for this equation has not yet been obtained. Generally, numerical techniques have been used instead [e.g., Rubin and Steinhardt, 1963; Freeze, 1969].

2.2. Shear Strength Variation in Partially Saturated Soils

The stability analyses of natural slopes require the evaluation of the destabilizing forces with respect to the shear strength of the soil, τ , and the variation of the shear strength itself [Lu and Godt, 2013]. According to the Mohr-Coulomb failure criterion, in a cohesionless soil the shear strength is proportional to the normal effective stress σ' [Terzaghi, 1943]:

$$\tau = \sigma' \cdot \tan \phi' = (\sigma - u_w) \cdot \tan \phi' \quad (2)$$

where ϕ' is the effective internal friction angle and σ is the total vertical stress. In defining the effective stress, Terzaghi only accounted for forces propagating through the soil skeleton. Given the practical relevance of the effective stress, many theoretical and practical studies have been undertaken to describe and quantify it. In particular, Bishop [1959], Skempton et al. [1960], Morgestern and Price [1965], and Fredlund and Morgestern [1977] followed a macroscale approach, which constitutes the basis of classical soil mechanics. Such an approach can accurately describe soil behavior under saturated conditions, when the soil-water system can be treated as an equivalent continuous medium with macroscopic stresses defined at the boundary. In this framework the pore water, which acts over the entire grain surface, constitutes a neutral, isotropic stress. Therefore, the system can be described by macroscopic stress-state variables such as total stress, pore water pressure, and intergranular bonding stress, which provides cohesion at zero normal stress. When the water content decreases and the soil begins to desaturate, however, the pore water pressure is no longer a neutral stress in the soil-water-air system. The macroscale variables are no longer adequate to describe the forces acting on the system since local interparticle forces arise through the different phases and their interfaces. According to Lu and Likos [2006], these forces are physicochemical forces, surface

tension, and forces arising from negative pore water pressure. Conceptually, they can be lumped together and described through a single macroscopic variable, σ^s called suction stress, which, together with the effect of air pressure acting on the dry, hydrated portion of the grain surfaces, u_a , can be added into Terzaghi's effective stress expression to account for interparticle forces in partially saturated soils. Therefore, the effective stress principle, under the framework of the suction stress characteristic curve [Lu and Likos, 2006] is expressed by equation (3):

$$\sigma' = (\sigma - u_a) - \sigma^s \tag{3}$$

and σ^s [see Lu and Likos, 2006] is defined in equation (4):

$$\sigma^s = \sigma_{C0} + \Delta\sigma_{pc} + \sigma_{cap} + \chi(u_a - u_w) \tag{4}$$

where σ_{C0} represents the physicochemical stress under saturated conditions, which is used as a reference, $\Delta\sigma_{pc}$ represents the changes in physicochemical stress due to desaturation, σ_{cap} is the capillary stress due to surface tension, and $\chi(u_a - u_w)$ describes the contribution due to matric suction. Matric suction, or simply suction, is defined as the difference between the air pressure acting on the dry portion of the grain surfaces and the pore water pressure, $(u_a - u_w)$. Of course, all of these local forces also exist in saturated soil but they are not necessary in describing the soil stress state, which can be fully described by macroscopic variables under saturated conditions. Since suction stress arises from soil desaturation, it is strongly dependent on water content and matric suction. As such, it is a characteristic function of the soil-air-water system that allows for the definition of the suction stress characteristic curve, SSCC (Figure 3). The suction stress is an intrinsic function of unsaturated soils that relates the resultant of interparticle physicochemical stresses, capillary stresses, and negative pore water pressure to the matric suction or to the water content [Lu and Likos, 2006]. It can be approximated by equation (5), Lu and Likos [2006], which underlines the dependence of suction stress on matric suction and relative saturation:

$$\sigma^s = -\frac{\theta - \theta_r}{\theta_s - \theta_r} (u_a - u_w) \tag{5}$$

In this respect, the suction stress approach provides a unified macroscopic representation of the microscopic behavior of unsaturated soils. Introducing equation (5) into the Mohr-Coulomb failure criterion yields:

$$\tau_f = c' + (\sigma_n - u_a)_f \tan \phi' + \frac{\theta - \theta_r}{\theta_s - \theta_r} (u_a - u_w)_f \tan \phi' \tag{6}$$

where c' is the cohesion at zero normal stress due to the intergranular bonding stress, σ_n is the total normal stress, u_a is the air pressure, u_w is the pore water pressure, and ϕ' is the internal friction angle. The term

$$c'' = \frac{\theta - \theta_r}{\theta_s - \theta_r} (u_a - u_w)_f \tan \phi' = -\sigma^s \tan \phi' \tag{7}$$

represents the apparent cohesion (i.e., the contribution of suction stress to soil shear strength, according to Lu and Likos [2006]).

There are various works in literature, such as [Meisina and Scarabelli, 2007; Montrasio and Valentino, 2008; Yeh and Lee, 2013; Lepore et al., 2013], that have used the effective stress equation for unsaturated soils based on the [Bishop, 1954] formulation $\sigma' = (\sigma - u_a) + \chi(u_a - u_w)$, where χ is a coefficient varying between 0 and 1. Most of these works have used the Vanapalli et al. [1996] parameterization ($\chi = \frac{\theta - \theta_r}{\theta_s - \theta_r}$). In this paper, however, we define the effective stress using the approach based on suction stress, [Lu and Likos, 2006]. This approach has unified the description of flow and stress phenomena in all types of soils, ranging from sand and silt to clay. Also, there is no need to define the coefficient χ for effective stress, given that suction stress is a function only of soil suction. Moreover, unlike previous formulations, the suction stress approach captures the nonlinear and peak behavior of the effective stress in sandy and silty soils.

2.3. The Relevance of the Suction Stress Approach to Slope Stability

The SSCC concept is applied to slope stability analysis to account for interparticle stresses that develop through changes in water content [Lu and Godt, 2008]. The soil strength required in the computation of the Factor of Safety (ratio of stabilizing to destabilizing forces), FS , is evaluated using equation (6), which has the following form when substituted:

$$\begin{aligned}
 FS &= \frac{\tan \phi'}{\tan \beta} + \frac{c'}{\gamma_s Z \sin \beta \cos \beta} + \frac{c''}{\gamma_s Z \sin \beta \cos \beta} \\
 &= \frac{\tan \phi'}{\tan \beta} + \frac{c'}{\gamma_s Z \sin \beta \cos \beta} - \frac{\sigma^s \tan \phi'}{\gamma_s Z \sin \beta \cos \beta} \\
 &= \frac{\tan \phi'}{\tan \beta} + \frac{c' + \frac{\theta - \theta_r}{\theta_s - \theta_r} \psi \gamma_w \tan \phi'}{\gamma_s Z \sin \beta \cos \beta}
 \end{aligned} \tag{8}$$

where β is the slope angle, ψ is the water potential [L], and Z is the soil thickness. Figure 1 provides an insight into rainfall-induced and stress-variation-induced soil failure mechanisms. Consider a natural, stable, unsaturated slope with an average stress state described by the larger Mohr circle (solid line) in Figure 1. Its failure envelope is represented by the straight line tangent to the solid Mohr circle. During a rainfall event, the soil imbibes water and suction stress is reduced, in line with variations in matric suction and volumetric water content. This corresponds to a downward shift of the failure envelope in Figure 1. Since the failure envelope in this configuration is secant to the larger circle (original solid line), the soil may fail.

This analysis of soil strength variations in hillslopes is expected to describe the evolution of slope stability without imposing a specific failure mechanism. It should also accurately reproduce shallow-landslide triggering times and locations.

3. The Hydrogeomechanical Model

Many variables and parameters are called into the formulation of equation (8): the slope angle, β , is determined by DEM analysis; the saturated unit weight, γ_s , is assigned after geological inspection; and soil thickness, Z , is given according to the hypotheses and models discussed in section 4. The friction angle, ϕ , and the cohesion coefficient, c' , are assumed as random variable, whose characteristics are described below. The assignment of the water-related parameters is also described below.

The soil water content, θ , and the suction, ψ , were simulated using the GEOTop model, [Rigon *et al.*, 2006; Endrizzi *et al.*, 2014]. Eventually, the simulated θ was considered as the mean value of a random variable too, as explained below.

By taking c' , ϕ , and θ to be random variables, we state our interest in the probability of failure (i.e., the probability of FS) rather than in FS itself, as given by equation (8). Assuming, therefore, that FS follows a log-normal distribution [Frattini *et al.*, 2009; Duncan, 2000] the probability of failure is:

$$P[FS < 1] = P[\ln FS < 0] = \Phi\left(-\frac{\mu_{\ln FS}}{\sigma_{\ln FS}}\right) \tag{9}$$

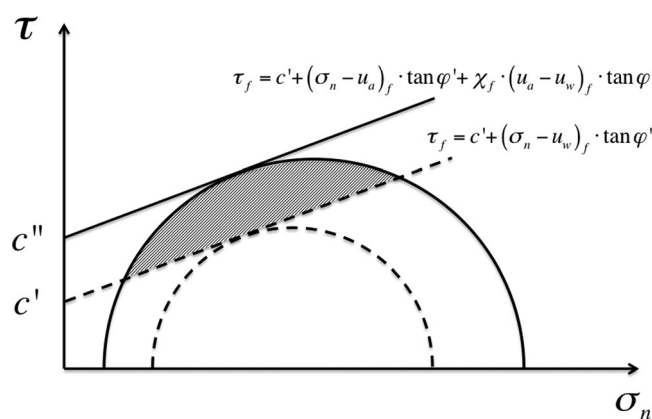


Figure 1. Schematic of Mohr circle showing a decrease in soil shear strength occurring during a rainfall event. The solid line circle represents the natural stress state of the slope before wetting, the dashed circle represents the minimum stress state occurring when the soil is saturated. c' is the cohesion due to the intergranular bonding stress and c'' is the apparent cohesion.

where: $\mu_{\ln FS} = (\ln \mu_{FS} - 0.5 \cdot \sigma_{\ln FS}^2)$; $\sigma_{\ln FS} = \sqrt{\ln(1 + v_{FS}^2)}$; μ_{FS} and v_{FS} are the mean and the coefficient of variation of FS computed using the FOSM method; and Φ is cumulative distribution function of the standard normal distribution. We assumed c' , ϕ , and θ as random variables with standard deviations equal to a percentage of the mean values.

The First-Order Second Moment Method (FOSM) [Dai and Lee, 2002; Baecher and Christian, 2005; Arnone *et al.*, 2015] is used here to approximate the expectation and variance of a function of independent random variables. It consists in approximating the

desired statistic, $G=G(x_1, \dots, x_n)$, with its Taylor series expansion about the expected (mean) values of random variables, so that:

$$E[G]=G(\mu[x_1], \dots, \mu[x_n]) \tag{10}$$

$$\sigma^2[G]=\sum_{i=1}^n \left(\frac{dG}{dx_i} \cdot \sigma[x_i] \right)^2 \tag{11}$$

where $\mu[x_i]$ and $\sigma[x_i]$ are, respectively, the mean and standard deviation of the random variable x_i .

Transient soil moisture, $\theta(t)$, and pressure heads, $\psi(t)$, are computed by numerically integrating the Richards equation with GEOTop, as described in *Endrizzi et al.* [2014]. In the model, equation (1) is discretized using a finite-volumes technique. The system of equations for each cell is solved by using a first-order precision, unconditionally stable, Newton-Krylov method. The required relation between suction head, ψ [L], and volumetric water content, θ [-], that is to say, the soil water characteristic curve (SWCC), is given through the *van Genuchten* [1980] parametrization.

The numerical integration of the Richards equation removes the assumption of stationary conditions in subsurface flows. Therefore, it is possible to describe infiltration-redistribution processes and consequent transient flows, which are of primary importance in landslide triggering.

For three-dimensional simulations, GEOTop is able to consider the influence of topography on water and energy budgets because it is based on a mesh directly derived from the digital elevation model (DEM) of the analyzed basin, which approximates natural slopes, aspect, and curvatures.

GEOTop and the estimation of failure probabilities are run by using different soil moisture conditions and pressure heads computed for each time step. This provides an FS probability that varies in time and space. In addition, the calculation is performed for each layer (into which the soil depth has been discretized) to investigate the stability at different depths, after having characterized the soil in geotechnical terms. Therefore FS probability also varies with depth, and the depth of a potential failure is allowed to vary from the surface to the bedrock without any constraint.

4. Model Application

To assess the impact of topography on transient hillslope hydrology and shallow landslide triggering, we consider three approximations of real topographies: concave, convex, and planar. They are extracted from 10 m DEM data of the Friuli region, in the eastern Italian Alps (Figure 2), using the uDig spatial toolbox, *Abera et al.* [2014]. The highly eroded character of the area is mainly due to a large landslide that occurred in 1817, *Castiglioni* [1962], in response to a heavy rainfall event. To isolate the effect of morphology, we assume a constant soil thickness of 1.5 m over the entire landscape, which is divided into 30 layers in the model. An impervious layer is located 1.5 m below the surface, at the base of the overlying soil. The three morphologies were selected based on their shape as seen from a 3-D rendering of the topography. Since the operator ∇^2z is the second derivative in space of the elevation (z , m) of a site, it represents the concavity/convexity of that site. Planar cells are the ones for which $\nabla^2z=0$, concave cells have $\nabla^2z > 0$ and convex cells have $\nabla^2z < 0$ [*Abera et al.*, 2014]. Individual hydrological and stability-analysis simulations were executed for each of the three different morphologies.

In the study area, many landslides have occurred during and after late summer storms, characterized by intense rainfall. Therefore, we carried out the analyses under similar conditions. We assumed a synthetic 12 h rainfall with an intensity of $I1 = 18$ mm/h, and we ran the simulations for 48 h. The hyetograph shape was assumed equal to the measured rainfall that triggered a landslide event in the study area. In order to understand the role and effect of the rainfall event, we also tested two different events with $I2 = 16$ mm/h and $I3 = 20$ mm/h, respectively, and both of 12 h duration. The rainfall intensity $I1$ should mimic a volume of rainfall that, on average, is both typical of this area of the Italian Alps and often triggers shallow landslides. Therefore, we chose an average value for the rainfall intensity within a typical 12 h event. With the aim of assessing infiltration pattern sensitivity to rainfall intensity, we explored two additional intensities $I2$ and $I3$. This choice was driven by a desire to investigate one variable at a time. Specifically, we wanted to investigate the role of morphology on infiltration and, ultimately, on the probability of failure. In the near future, the role of rainfall intensity in this matter will be further investigated in its own right.

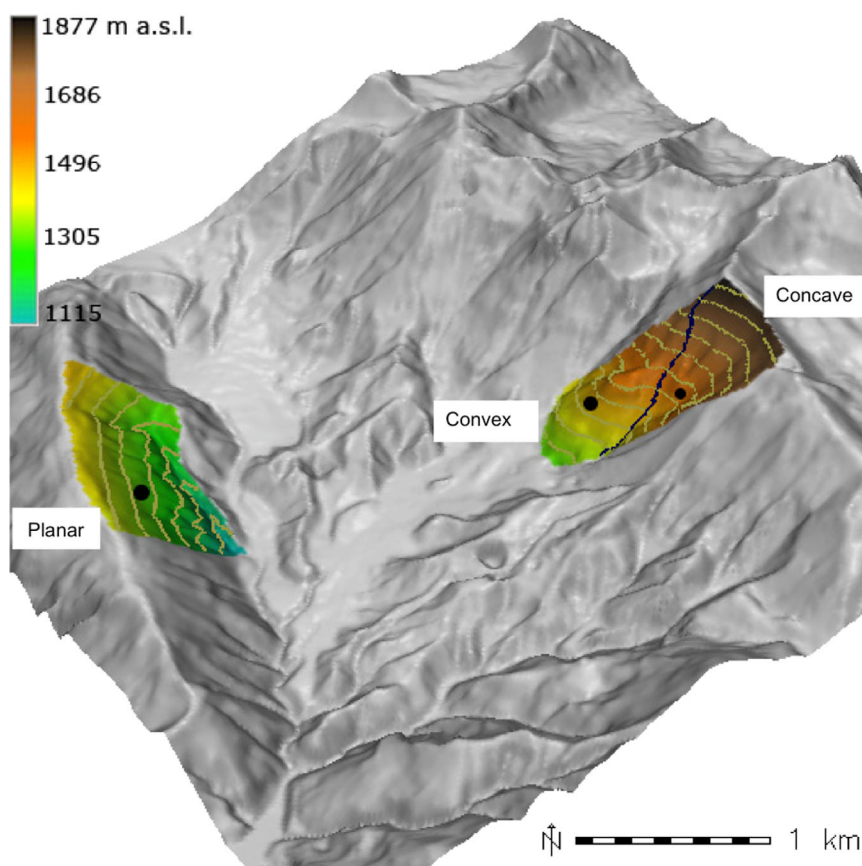


Figure 2. Model domain for basin-scale simulations shown on 10 m resolution, shaded relief map. The representative hillslopes selected for morphological analysis are highlighted in color and labeled. Basin wide elevation ranges from 1000 to 1900 m above sea level. Friuli, Italy.

Three different water table depths were set as initial conditions to assess the impact of the antecedent soil moisture conditions. Water table depths at 1.7, 2.0, and 2.5 m below the surface define the Wet, Medium, and Dry initial conditions, respectively. Based on the water table depth, GEOtop computes a hydrostatic profile of initial water pressure for the unsaturated zone. Water content is computed accordingly, using a soil water retention curve relationship. For all simulations, the soil has a cohesion of 5 kPa and an internal friction angle of $\phi' = 34$. The soil unit weight varies with depth according to the water content of each layer under initial conditions, then it is allowed to vary according to the variation in water content. The soil is a homogeneous silty sand, characterized by a 10^{-5} m/s saturated hydraulic conductivity and van Genuchten parameters of $n = 3.5$, $\alpha = 0.97 \text{ m}^{-1}$, $\theta_r = 0.02$, $\theta_s = 0.4$ [van Genuchten, 1980]. The soil water characteristic curve (SWCC) and the soil stress characteristic curve (SSCC) are shown in Figure 3, left-hand and right-hand sides, respectively. Soil parameters have been derived from laboratory tests on specimens sampled at the experimental site. Direct shear tests under field conditions were used to determine the shear strength parameters of the soils. Standard deviation is used to describe test result variability.

Even though GEOtop is able to simulate infiltration excess overland flow, this runoff mechanism is not the main process taking places in the study area. In fact, the soil types are characterized by saturated hydraulic conductivity (36 mm/h), higher than the three rainfall intensities used in the simulations (I1 = 18 mm/h, I2 = 16 mm/h, and I3 = 20 mm/h). Because the three rainfall intensities are each applied for 12 h, each scenario has a different rainfall total input: 216 mm for I1, 192 mm for I2, and 240 mm for I3. Finally, during the simulation period, we neglected the evapotranspiration effect on the water content dynamic.

5. Simulation Results

The hydrological model, GEOtop, yields maps of pressure head and volumetric moisture content at hourly time steps for each morphology analyzed. The probabilistic infinite-slope stability model, based on the FOSM

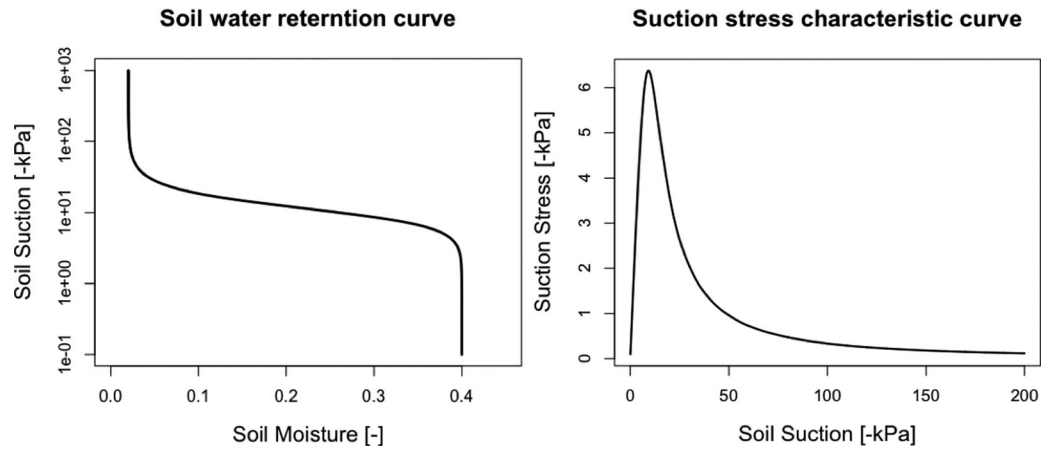


Figure 3. Soil water characteristic curve (left: SWCC) and suction stress characteristic curve (right: SSCC) [Lu and Likos, 2006] for the homogeneous soil of the case study. The relative van Genuchten parameters are $n = 3.5$, $\alpha = 0.97 [m^{-1}]$, $\theta_r = 0.02$, $\theta_s = 0.4$.

method, yields stability maps in terms of probability of failure. Pressure head, water content, and stability maps are output at hourly time steps. We did not use observed soil moisture time-series to evaluate the simulated soil moisture dynamics. In the next subsections, we describe: (i) the influence of morphology on transient hydrology at local and catchment scales, considering rainfall I1 and initial condition Medium, (ii) the influence of morphology on probability of failure considering rainfall I1 and initial condition Medium, and (iii) the influence of hyetographs (I1, I2, and I3) and initial conditions (WET, MEDIUM, AND DRY) on probability of failure.

5.1. Impact of Morphology on Transient Hydrology

Figure 4 shows the effects of infiltration on pore water pressure at three locations (P1, P2, and P3) for each of the concave, convex, and planar morphologies. The three points were selected in the upper (P1), middle

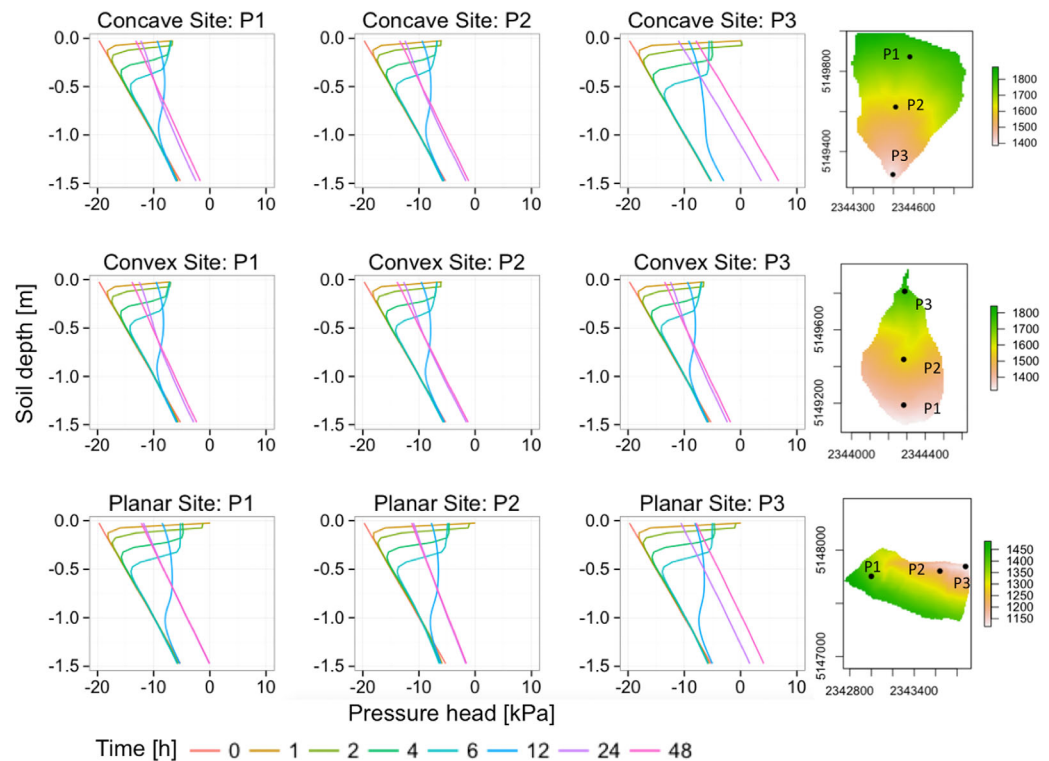


Figure 4. Pressure head profiles evolution in time at three given locations (P1, P2, and P3) for concave, convex, and planar topographies, respectively. Different colors represent different time steps (0, 1, 2, 4, 6, 12, 24, 48 h from simulation start). The color variation in the maps represents the elevation in meters.

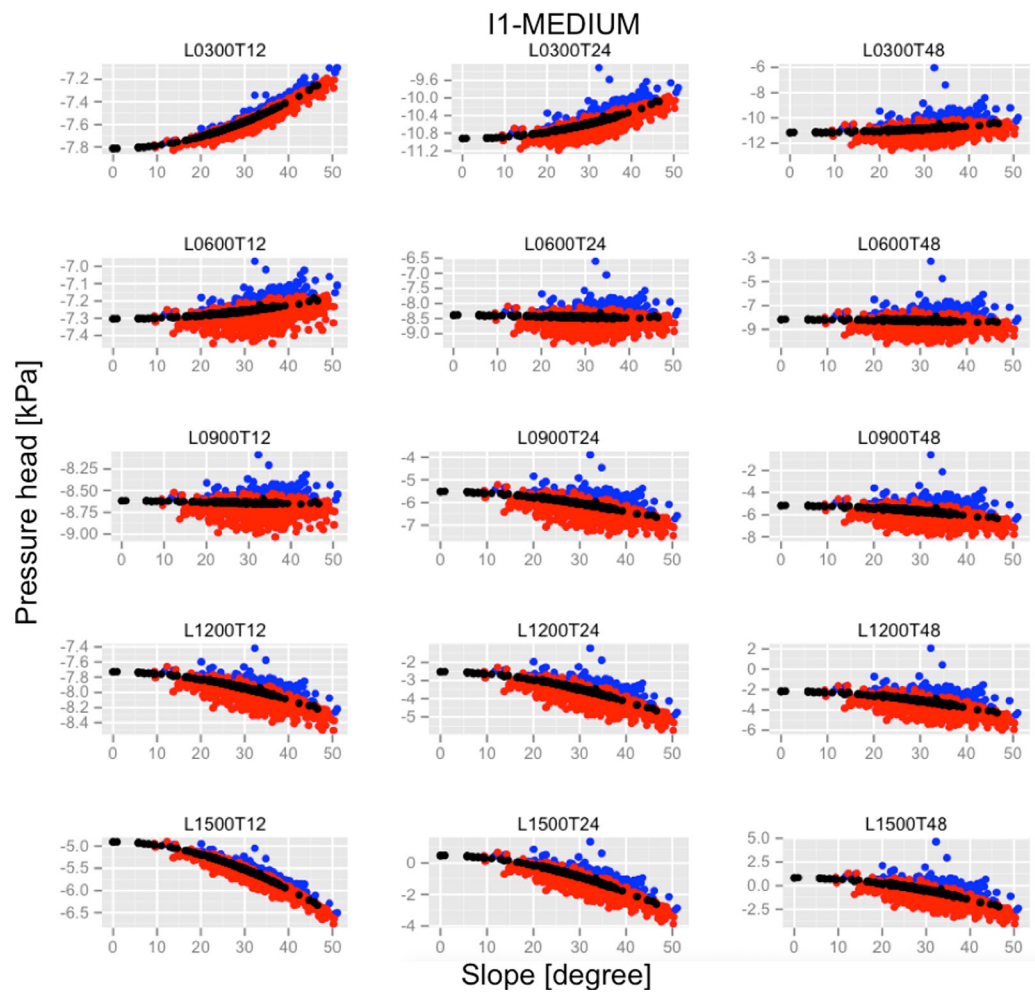


Figure 5. Evolution of pressure head as a function of slope for concave, convex, and planar morphologies, respectively in blue, red and black dots. Plots are provided for different soil layers (0.3, 0.9, 1.2, and 1.5 m deep) and for different time steps (12, 24, 48 h from simulation start). Each row represents a given soil layer and each column represents a given time step. Each single plot is labeled: L stand for layer, followed by the depth of the layer, T stands for time followed by the time at which the plot is referred.

(P2), and lower (P3) parts of the basins and have similar hydrological and topographic features (total contributing area, slope angle, topographic gradient, soil properties). Soil moisture profiles for the same points are reported in supporting information Figure S1. Infiltration profiles for the different basin morphologies are generally similar in shape and values. This is more evident during the initial part of the simulation and for the upper locations (P1); while during the final part of the simulation and for the lower locations (P3) the pressure head in the concave morphology assumes slightly higher values than in the convex morphology. Moreover, in supporting information Figures S4–S6 we presented the relationship between pressure head and slope for each morphology filtered by the logarithm of the total contributing area. The figures show that the differences between morphologies appear more evident by increasing the total contributing area and that below 0.01 km² the behavior of the three morphologies is quite similar. This confirms that, at local scale, topography has little impact on transient hydrology (at least this is true for the representative morphologies and locations selected, i.e., the points P1, P2, P3 on each slope). This is because the flow in the unsaturated zone is mainly vertical (as stated in Iverson [2000]; Lu et al. [2011]) and not affected by later redistribution.

In contrast, an effect is observed at the catchment scale (Figure 5 and supporting information Figure S2), where pore pressure and water content distributions vary as a function of the slope angle for concave, planar, and concave morphologies. In Figure 5 and supporting information Figure S2, each row refers to a soil layer (0.3, 0.9, 1.2, and 1.5 m deep, respectively) and each column refers to a time step (12, 24, 48 h from

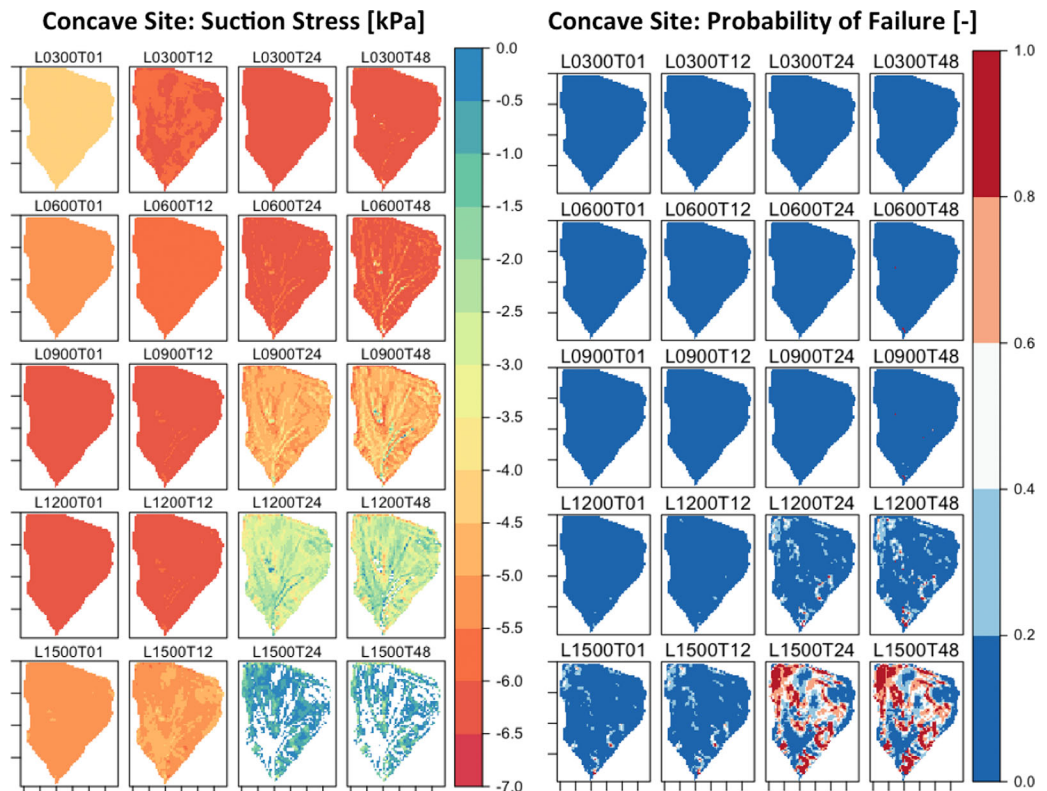


Figure 6. Suction stress and probability of failure pattern evolution for the concave site. Plots are provided for different soil layers (0.3, 0.6, 0.9, 1.2, and 1.5 m deep, respectively) and for different time steps (1, 12, 24, 48 h from simulation start). Each row represents a given soil layer and each column represents a given time step. Each plot is labeled: L stands for layer, followed by the depth of the layer, and T stands for time, followed by the time step, to which the plot is referred.

simulation start). In the figures, the blue, red, and black points correspond to cells of the concave, convex, and planar morphologies, respectively.

For a given slope angle, positive pressure heads and water content are higher for the concave morphology (blue points) than for the planar (black points) and convex (red points) morphologies, respectively. Differences in pore water pressure and in soil water content increase with simulation time and with slope. This highlights that, although concave morphologies are more prone to collect water than steep morphologies, the effect of morphology on infiltration and redistribution is quantitatively minimal, particularly in the upper vadose zone. Since, as shown, pressure head values are locally independent of the morphology, differences in pressure heads at catchment scale, can be attributed to saturated, lateral, subsurface flow. Moreover, the topographic effect is emphasized in steeper slopes, when the lateral distribution is more significant and consequently the terrain shape becomes more important.

5.2. Relation Between Changes in Suction Stress and Failure Probability

Figures 6 and 7 show the spatial correlation between changes in suction stress and probability of failure for the concave and convex sites, respectively. Results are reported for five layers (at 0.3, 0.6, 0.9, 1.2, and 1.5 m depth, respectively) and four time steps (1, 12, 24, and 48 h after the storm beginning). White areas in the suction stress maps represent the portion of the catchment which is saturated, where the suction stress reduces to zero; colored pixels are unsaturated points, whose value is readable from the color-key. Corresponding patterns of instability are illustrated in the maps on the right-hand side in terms of probability of failure. Therefore, red zones in the stability map are associated with a high probability of failure (80–100%), are saturated or near saturation and their relative suction stress is negligible. The suction stress maps in Figures 6 and 7 provide insight into the possible triggering mechanism occurring in this particular case. The shallow layers, less than 60 cm, do not experience significant increases in soil moisture compared to the deeper layers at any time step of analysis. This suggests that the increase in soil moisture in deeper layers

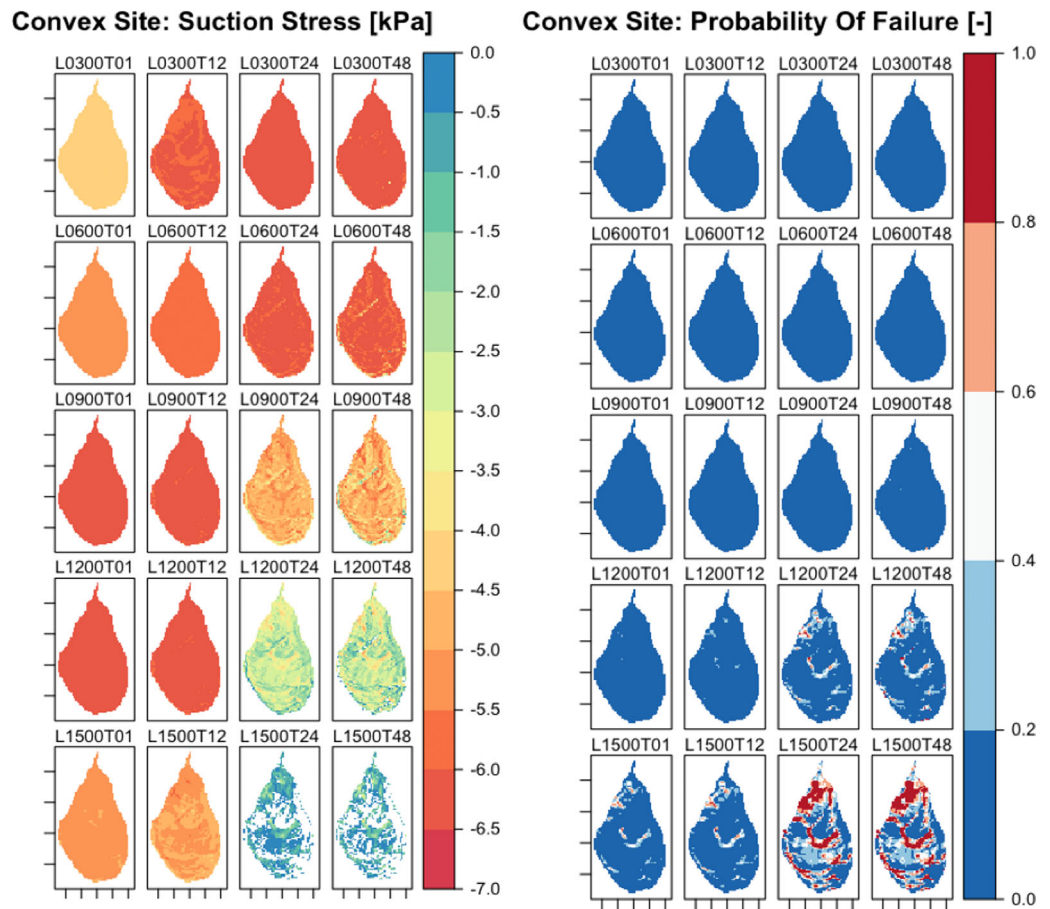


Figure 7. Suction stress and probability of failure pattern evolution for the convex site. Plots are provided for different soil layers (0.3, 0.6, 0.9, 1.2, and 1.5 m deep, respectively) and for different time steps (1, 12, 24, 48 h from simulation start). Each row represents a given soil layer and each column represents a given time step. Each plot is labeled: L stands for layer, followed by the depth of the layer, and T stands for time, followed by the time step, to which the plot is referred.

may, for the most part, originate from lateral redistribution. Suction stress, which is tensile in nature (negative values), increases (from negative values toward 0) as the soil wets and vanishes when the soil becomes completely saturated. As a consequence, shallow landslides result from a relatively rapid increase in soil suction, which reduces soil strength. Figure 8 shows the probability of failure as function of the slope angle for the 1.2 m layer and the 48 h time step for the convex and concave sites. The colors of the points indicate its suction stress value. The figure shows how, for a given slope, saturated or near-saturated pixels have a higher probability of failure compared to unsaturated pixels. This trend is evident for pixels with slope angle greater than 25° , both in concave and in convex sites.

5.3. Impact of Basin Morphology on Slope Stability

To assess the impact of morphology on slope stability, we quantify the propensity for shallow landslide occurrence as a function of the slope angle, which is the gradient of the elevation function at any given point. Analyses were carried out for each basin morphology type: concave, convex, and planar. Stability analysis focuses on determining the factors causing landslide triggering (wetness, time, depth, soil geo-mechanical characteristics, etc.). The layering used is a means of discretizing soil depth: slope failure probability is computed independently of each soil layer to identify the weakest depth at which the column of soil above that depth would fail. For this reason, as soon as instability occurs in a certain layer of soil we consider the whole hillslope unstable, even if the shallow layers remain stable. The percentage of unstable areas is computed as the ratio of the area characterized by a probability of failure higher than 0.75 to the total area of the basin (with area calculated as number of pixels times pixel resolution).

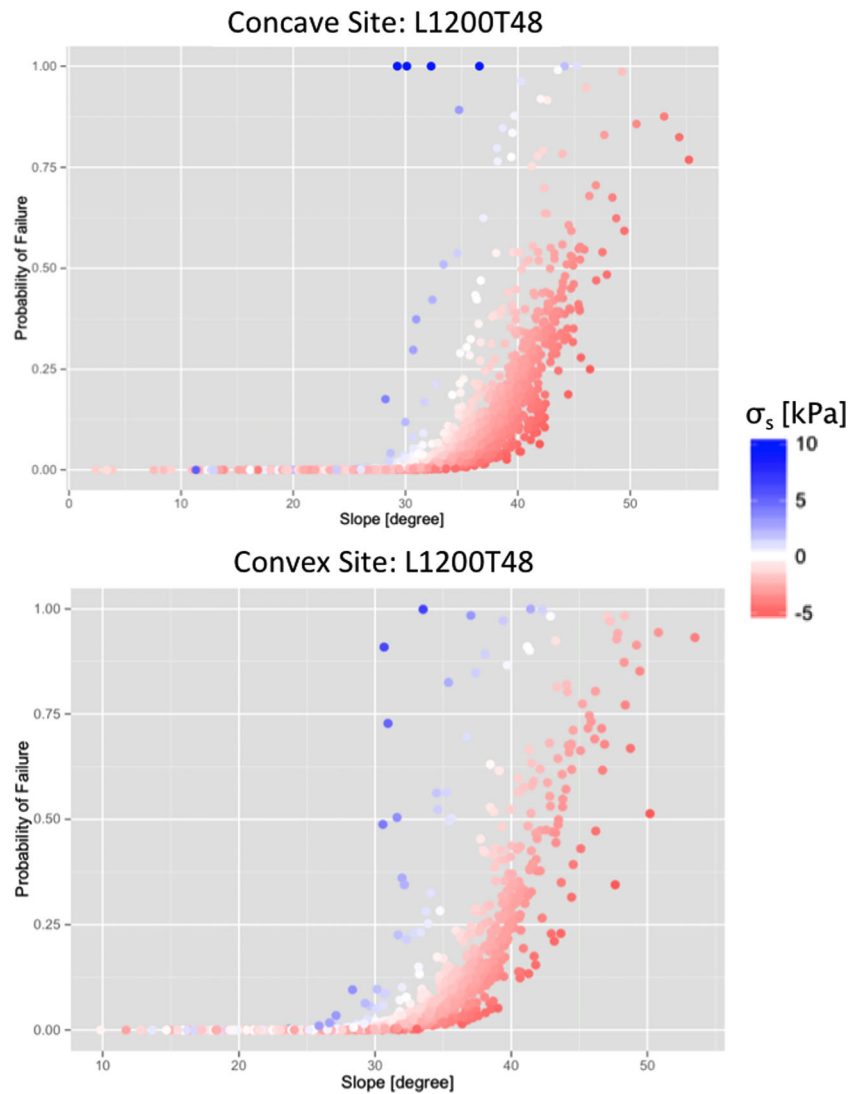


Figure 8. Probability of failure in the concave and convex sites as a function of the slope angle for the 1.2 m layer and at the 48 h time step. The colors of the points represent the suction stress value.

Figure 9 shows the probability of failure as a function of the slope angle for concave, planar, and convex basin morphologies. Each row refers to a soil layer (0.3, 0.9, 1.2, and 1.5 m deep) and each column refers to a time step (12, 24, 48 h from simulation start). Instability occurs at 1.2 m depth and 24 h after the beginning of simulation for concave sites. At 1.5 m depth, all three morphologies are unstable; even in this case, however, for a given slope, concave sites have a higher probability of failure.

In general, the failure probability is higher for the concave morphology and this behavior is more evident as the slope increases. A concave basin morphology can be more vulnerable to shallow landslides than a planar or convex site due to lateral fluxes that are topographically driven toward concave areas. To test the validity of this statement, we computed the percentage of saturated area for the three basin morphologies at 1.2 m depth and 24 h after the beginning of simulation. We used 1.2 m depth because it is the depth where failure occurred.

Results show that the 32% of the concave basin was saturated versus 27.6% of the convex and 29.7% of the planar sites. Concave sites are, therefore, prone to collect and store soil moisture, which allows for a greater increase in pore-water pressure at the impermeable lower boundary and an increase in the area resulting unstable in the model. This is also confirmed by the percentage of unstable area of each site computed at 1.5 m depth for time step 24 h: percentage of unstable areas is equal to 30, 21, and 1.3%, for concave,

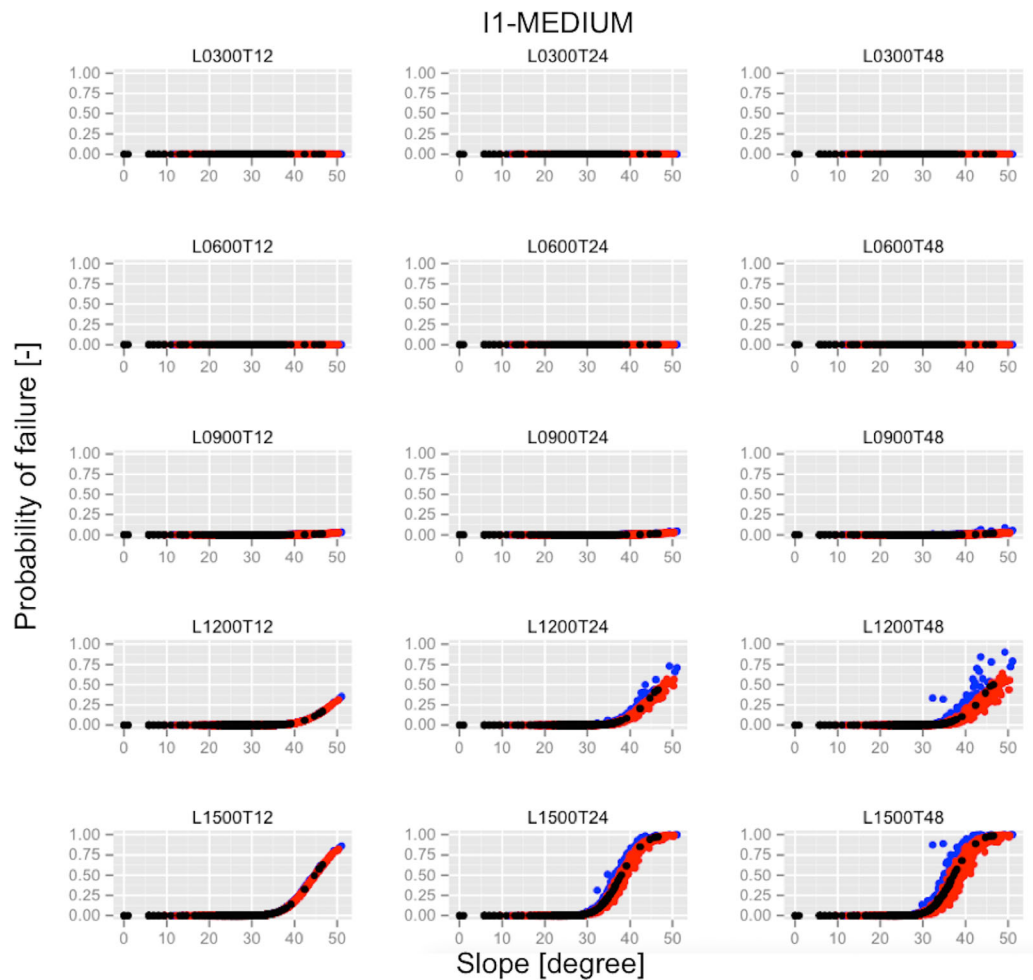


Figure 9. Evolution of probability of failure as function of the slope for the concave, convex, and planar morphologies, respectively in blue, red, and black dots. Plots are provided for different soil layers (0.3, 0.6, 0.9, 1.2, and 1.5 m deep, respectively) and for different time steps (12, 24, 48 h from simulation start). Each row represents a given soil layer and each column represents a given time step. Each plot is labeled: L stands for layer, followed by the depth of the layer, and T stands for time, followed by the time step, to which the plot is referred.

convex, and planar basin morphologies, respectively. Both in the concave and in convex morphologies, we found high probability of failure in the upslope parts of the basins. This is explained by high slope angles in those parts of the basins.

5.4. Impact of Rainfall and Initial Conditions on Slope Stability

The results presented in the previous subsections are for the Medium initial condition (water table depth at 2.0 m) and the I1 (18 mm/h) rainfall rate. In order to investigate the effect of initial conditions and rainfall rate on slope stability, simulations were also conducted using I2 (16 mm/h) and I3 (20 mm/h) rainfall rate and Wet (water table depth at 1.7 m) and Dry (water table depth at 2.5 m) initial conditions. Following the same procedure presented in the previous section, the percentage of unstable areas is computed for each scenario by combining each hyetograph (I1, I2, and I3) with each initial condition (Dry, Medium, and Wet). Comparisons of the percentage of unstable areas computed for the nine scenarios are presented in Figure 10 for the 24 h time step. A single plot in Figure 10 shows the percentages of unstable area (y axis) for different hyetographs (x axis) and for different morphologies: concave (in blue), convex (in red), and planar (in black). Figure 10 has five rows, one for each soil layer (at 0.3, 0.6, 0.9, 1.2, and 1.5 m depth) and has three columns, one for each analyzed initial condition (Dry, Medium, and Wet).

In all scenarios, the percentage of unstable areas for the concave site is higher than those for the convex and planar morphologies. For the scenarios based on Dry initial condition, unstable areas are less than 1%

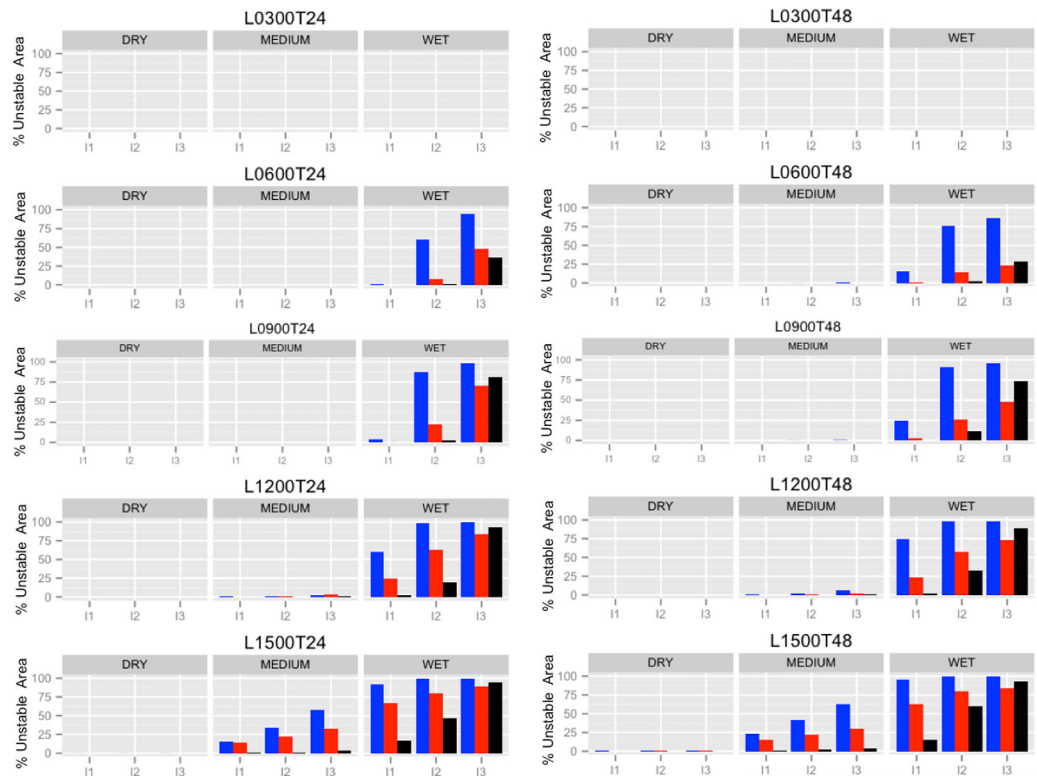


Figure 10. Comparison between percentages of unstable areas computed for time step 24 h. The figure shows the percentage of unstable area (y axis) for different hyetographs (I1, I2, and I3) and for different morphologies: concave (in blue), convex (in red), and planar (in black). Each row of the figure refers to a different soil layer (at 0.3, 0.6, 1.2, and 1.5 m depth) and each column refers to a different initial condition considered (DRY, MEDIUM, and WET).

for all the three morphologies and for each rainfall scenario. For the scenarios based on Medium initial condition, the percentage of unstable areas increases with rainfall. Moving from 16 to 20 mm/h, the increase of unstable areas is higher for concave sites (from 30% to 55%) than for convex sites (from 21% to 30%).

The scenarios based on the Wet initial condition are the most landslide prone. Instability occurs at 0.6 m depth for almost all the basin morphologies and involves a greater portion of the basins compared to the results based on Medium scenarios. The lowest intensity rainfall (16 mm/h) combined with the Wet initial condition triggers instability after 24 h and at 1.2 m of depth. In this case, percentage of unstable areas is more than 50% for concave morphology, almost 25% for the convex and 1% for the planar.

5.5. Discussion

The results of this study provide an accurate numerical investigation of how different morphologies effect variable saturated hillslope hydrology and shallow slope stability. This was previously assessed just by field measurements and/or empirical models [e.g., *Dai and Lee, 2002; Carrara et al., 2003; Dahal et al., 2008*].

Our analysis was not limited to a steady state description of subsurface flows and allowed therefore to evaluate the timing of the failure and the role played by transient rainfall and antecedent soil moisture conditions. For control, we also performed a slope stability simulation based on the SHALSTAB model [*Dietrich and Montgomery, 1994*] presented and commented in the complimentary material. These simulations confirm the overestimation of the unstable areas that was previously observed in other works [e.g., *Casadei et al., 2003; Lanni et al., 2011*]. Literature and our own analysis agree in attributing this overestimation to the simplification of fluxes dynamics and to the stabilizing effect of soil cohesion and suction stress which SHALSTAB does not account for.

Differently from previous studies [e.g., *Mirus et al., 2007; Simoni et al., 2008; Arnone et al., 2015*], we used a three-dimensional hydrological model for solving the Richards equation, carefully modify to manage transition from vadose to saturated conditions, and we implemented the effective stress theory by *Lu and Likos*

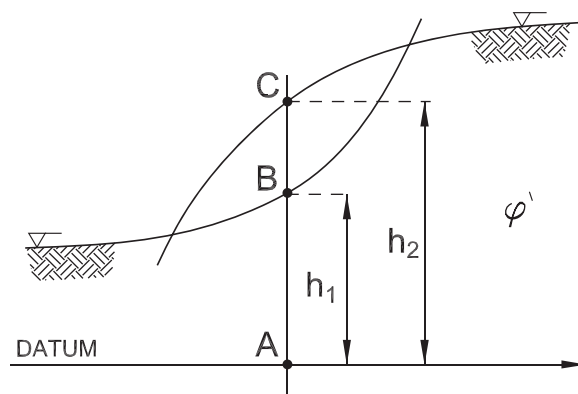


Figure 11. Schematic of the different overburden stresses for concave and convex morphologies. $h_1 = AB$ and $h_2 = AC$ represent the soil thickness above a given horizontal datum for a concave and a convex slope, respectively.

[2006] that provides a unified and mathematically consistent description of transition between saturated and unsaturated states.

The hydrological analysis suggests that, in a silty sandy soil for the selected rainfall rates (16, 18, and 20 mm/h, each with a duration of 12 h), and initial and boundary conditions, infiltration is not greatly affected by morphology at local scale. Because the water table rises during the storm event, the saturated zone expands upward, generating a saturated flow that moves downslope. This results in an increase in the soil moisture content of areas located downslope that is not only due to rainfall infiltration, but also to saturated subsurface flows that flow from the catchment crest toward the basin outlet.

The results presented in this paper show that transient pressure heads influence the stress state of soil, inducing variations in suction stress. In particular, the results indicate that a decrease in the absolute value of suction stresses, due to an increase in pressure head, may induce shallow soil failures. Rainfall infiltration increases water content and, as a consequence, the absolute values of both soil suction and suction stress decrease. However, changes in the stress field only involve shear strength, since the variations in suction stress are small compared to the vertical effective stress [Terzaghi, 1943]; in addition, the lateral component of the earth pressure, being proportional to the vertical effective stress, is not significantly affected by these changes. This aspect is captured by the numerical solution of the Richards equation implemented in the model; in contrast, the infinite-slope approach does not describe the effects of morphology on slope stability as far as the 3-D stress field is concerned. A 3-D slope stability approach should also account for neighboring effects on the stability of a single cell due to lateral earth pressure. This would provide insight into the effects of morphology on the 3-D stress field, showing that, at a given point within the soil mantle, the contribution of the lateral earth component is larger for a convex slope than for a concave one (Figure 11) because of the greater vertical overburden stress, $\sigma_v = \gamma_{soil} \cdot h_i$, generated by a larger soil thickness laying above a given horizontal datum in a convex slope ($AC = h_2$) than in a concave one ($AB = h_1 < h_2$). This has two opposing consequences, the balancing of which dictates the stability of a given location. Since the lateral earth pressure is added to the downslope weight component, it plays a more destabilizing role in a convex morphology than in a concave one. The counterpart is relative to the soil shear strength, which is proportional to the vertical effective stress $\sigma'_v = \sigma_v - u_w$, being u_w the pore water pressure [Terzaghi, 1943]. Therefore, given the same overall conditions, the shear strength of a soil in a convex morphology is higher than in a concave morphology. However, in this case the effect of morphology would be practically time-independent due to small value of changes to suction stress relative to the vertical effective stress (overburden stress). If the variation of the earth pressure coefficient with matric suction were considered [Lu and Likos, 2004], then the lateral earth pressure would be theoretically time-dependent.

A constant soil thickness was assumed regardless of the basin morphology, so that morphological effects are investigated with respect to subsurface fluxes only. The effect of morphology on soil thickness is deliberately ignored in this study and the results have been interpreted in this context. They do not claim general validity since they have been found under specific hydrological conditions and for specific morphologies.

The right-hand side of Figure 3 shows the relation between soil suction (negative pressure head) and suction stress for the silty sand investigated in this work. The curve presents a peak at 1 kPa of soil suction. This indicates that there is an optimum value of water content that maximizes the soil strength, providing 6.25 kPa of apparent cohesion. The slope is initially stable under the initial water content, which provides the slope with around 4.5 kPa of minimum apparent cohesion. This value is computed considering the maximum water content of the initial condition (0.35), which corresponds to the minimum value of apparent soil cohesion.

Moreover, in order to show that results are not dependent on the value of rainfall intensity and initial conditions used for the simulations, we analyzed the sensitivity of unstable areas to these quantities. The results confirmed that the percentage of unstable areas for the concave site is higher than that for convex and planar morphologies for all scenarios.

6. Conclusions

An analysis was carried out on three different basin morphologies, derived from a 10 m DEM, to investigate the impact of basin morphology on partially saturated, transient hydrology at catchment scale and, ultimately, on slope stability. This analysis suggests that the impact of morphology on transient hydrology is scale-dependent. As shown, it is not greatly relevant at local scale for points having the same hydrological features (total contributing area, distance from the divide, slope angle, hydraulic conductivity, van Genuchten parameters), where pressure head and water content profiles are nearly identical (Figure 4 and supporting information S1). Whereas some more relevant impacts are observed at catchment scale, as displayed by the right-hand side of Figure 5 and supporting information Figure S2. Slope stability is affected by: (i) a decrease in soil suction throughout the whole catchment during a rainfall event; and (ii) by higher water pressures that build up at concave locations, where water is topographically driven through saturated subsurface flows. A transient 3-D numerical simulation has the potential to capture lateral flows and lateral redistribution of soil moisture both in the short and long-term. The landslide triggering time can be predicted more reliably through an improved description of the pressure redistribution. This can be done by incorporating the effect of the unsaturated zone and by implementing a probabilistic approach, which provides failure patterns and probability, as presented in Figures 6 and 7.

Additionally, the study shows the correlation between a decrease in soil effective stress and slope instability, providing a physical explanation for the shallow landslides that are often observed during and after high-intensity storms. In steep slopes (with internal friction angle greater or similar to the slope angle), where the soil is held in place by capillarity (tensile suction stress), an increase in soil moisture content, due to rainfall infiltration, may build pore water pressure and reduce the soil shear strength. Results show that, despite partially saturated subsurface flow not being affected significantly by morphology at local scale, morphology has an effect on the total subsurface flow and on slope stability at catchment scale.

The infinite-slope assumption, implemented in the model, neglects mechanical effects of three-dimensional landslide geometry. This introduces an approximation which could bias the physical understanding of shallow landslide triggering. Further effort is required to advance the physical understanding of shallow landslide triggering at watershed scale in a fully 3-D, time-dependent context.

Last, future work could examine the effects resulting from the hydraulically anisotropic character of soils; methods could include observations of soil water content and suction. Indeed, the results provided in the paper may be used to guide future monitoring efforts, needed to provide a more comprehensive validation of the results and conclusions reported.

Acknowledgments

The First author is grateful to the USGS Geological Hazards Science Center for hosting him in Golden, CO, and for its scientific support. The authors also thank the editor and the reviewers for their constructive comments, which helped us to improve the manuscript. Data used in this research can be provided by contacting formetta@mines.edu.

References

- Abera, W., A. Antonello, S. Franceschi, G. Formetta, and R. Rigon (2014), The uDig Spatial Toolbox for hydro-geomorphic analysis, in *Geomorphological Techniques*, edited by L. Clarke, and J. Nield, Brit. Soc. for Geomorphol., London, U. K.
- Arnone, E., Y. G. Dialynas, L. V. Noto, and R. L. Bras (2015), Accounting for soils parameter uncertainty in a physically-based and distributed approach for rainfall-triggered landslides, *Hydrol. Processes.*, *30*, 927–944, doi:10.1002/hyp.10609.
- Baecher, G. B., and J. T. Christian (2005), *Reliability and Statistics in Geotechnical Engineering*, John Wiley, Hoboken, N. J.
- Baum, R., J. Godt, and W. Savage (2010), Estimating the timing and location of shallow rainfall-induced landslides using a model for transient, unsaturated infiltration, *J. Geophys. Res.*, *115*, F03013, doi:10.1029/2009JF001321.
- Bear, J. (1972), *Dynamics of Fluids in Porous Media*, Elsevier, Dover, N. Y.
- Beville, S., B. Mirus, B. Ebel, G. Mader, and K. Loague (2010), Using simulated hydrologic response to revisit the 1973 lerida court landslide, *Environ. Earth Sci.*, *61*(6), 1249–1257.
- Bishop, A. W. (1954), The use of pore-pressure coefficients in practice, *Geotechnique*, *4*(4), 148–152.
- Bishop, A. W. (1959), The principle of effective stress, *Tecknisk Ukeblad I Samarbeide Med Teknisk*, *106*(39), 859–863.
- Capparelli, G., and P. Versace (2011), Flair and sushi: Two mathematical models for early warning of landslides induced by rainfall, *Landslides*, *8*(1), 67–79.
- Carrara, A., G. Crosta, and P. Frattini (2003), Geomorphological and historical data in assessing landslide hazard, *Earth Surf. Processes Landforms*, *28*(10), 1125–1142.
- Casadei, M., W. Dietrich, and N. Miller (2003), Testing a model for predicting the timing and location of shallow landslide initiation in soil-mantled landscapes, *Earth Surf. Processes Landforms*, *28*, 925–950.

- Castiglioni, G. (1962), Chapter: L'erosione attuale nella conca di Sauris (Carnia), in *Aspetti Geografici Dell'erosione Del Suolo in Italia*, pp. 199–220, CNR Centro di Studi per Geogr. Fis.: Atti del 18. congresso geografico italiano : Trieste, 4-9 aprile 1961 / Comitato permanente dei congressi geografici italiani, Trieste: Istituto di Geografia dell'Università, 1964.
- Dahal, R. K., S. Hasegawa, A. Nonomura, M. Yamanaka, T. Masuda, and K. Nishino (2008), Gis-based weights-of-evidence modelling of rainfall-induced landslides in small catchments for landslide susceptibility mapping, *Environ. Geol.*, *54*(2), 311–324.
- Dai, F. C., and C. F. Lee (2002), Landslide characteristics and slope instability modeling using gis, lantau island, Hong Kong, *Geomorphology*, *42*(3), 213–228.
- Dai, F. C., C. F. Lee, and Y. Y. Ngai (2002), Landslide risk assessment and management: An overview. *Eng. Geol.*, *64*(1), 65–87.
- Dietrich, W. E., and D. Montgomery (1994), A physically based model for the topographic control on shallow landsliding, *Water Resour. Res.*, *30*(4), 1153–1171.
- Dietrich, W. E., C. J. Wilson, and S. L. Reneau (1986), Hollows, colluvium and landslides in soil-mantled landscapes, in *Hillslope Processes, Sixteenth Annual Geomorphology Symposium*, edited by A. Abrahams, pp. 361–388, Allen and Unwin.
- Dietrich, W. E., D. Bellugi, A. M. Heimsath, J. J. Roering, L. Sklar, and J. D. Stock (2003), Geomorphic transport laws for predicting the form and evolution of landscapes, in *Prediction in Geomorphology, AGU Geophys. Monogr. Ser. vol. 135*, edited by P. Wilcock and R. Iverson, pp. 103–132, AGU, Washington, D. C.
- D'Odorico, P., and R. Rigon (2003), Hillslope and channel contributions to the hydrologic response, *Water Resour. Res.*, *39*(5), 1113, doi:10.1029/2002WR001708.
- Duncan, J. M. (2000), Factors of safety and reliability in geotechnical engineering, *J. Geotech. Geoenviron. Eng.*, *126*(4), 307–316.
- Ebel, B. A., K. Loague, and R. I. Borja (2010), The impacts of hysteresis on variably saturated hydrologic response and slope failure, *Environ. Earth Sci.*, *61*(6), 1215–1225.
- Endrizzi, S., S. Gruber, M. Dall'Amico, and R. Rigon (2014), Geotop 2.0: Simulating the combined energy and water balance at and below the land surface accounting for soil freezing, snow cover and terrain effects, *Geosci. Model Dev.*, *7*(6), 2831–2857.
- Frattoni, P., G. Crosta, and R. Sosio (2009), Approaches for defining thresholds and return periods for rainfall-triggered shallow landslides. *Hydrol. Processes*, *23*(10), 1444–1460.
- Fredlund, D. G., and N. Morgestern (1977), Stress state variable for unsaturated soils, *J. Geotech. Eng. Div. Am. Soc. Civ. Eng.*, *103*(GT5), 447–466.
- Freeze, R. A. (1969), The mechanism of natural ground-water recharge and discharge 1. One-dimensional, vertical, unsteady unsaturated flow above a recharging or discharging ground-water flow system, *Water Resour. Res.*, *5*(1), 153–171.
- Heimsath, M. A., W. E. Dietrich, K. Nishiizumi, and R. Finkel (1997), The soil production function and landscape equilibrium, *Nature*, *388*, 358–361.
- Iverson, R. M. (2000), Landslide triggering by rain infiltration, *Water Resour. Res.*, *36*(7), 1897–1910.
- Lanni, C., J. McDonnell, and R. Rigon (2011), On the relative role of upslope and downslope topography for describing water flow path and storage dynamics: A theoretical analysis, *Hydrol. Processes*, *25*, 3909–3923.
- Lanni, C., M. Borga, R. Rigon, and P. Tarolli (2012), Modelling catchment-scale shallow landslide occurrence by means of a subsurface flow path connectivity index, *Hydrol. Earth Syst. Sci. Discuss.*, *9*, 4101–4134.
- Lepore, C., E. Arnone, L. Noto, G. Sivandran, and R. Bras (2013), Physically based modeling of rainfall-triggered landslides: A case study in the luquillo forest, puerto rico, *Hydrol. Earth Syst. Sci.*, *17*(9), 3371–3387.
- Lu, N., and J. Godt (2008), Infinite slope stability under steady unsaturated seepage conditions, *Water Resour. Res.*, *44*, W11404, doi: 10.1029/2008WR006976.
- Lu, N., and J. W. Godt (2013), *Hillslope Hydrology and Stability*, Cambridge Univ. Press, U. K.
- Lu, N., and W. J. Likos (2004), *Unsaturated Soil Mechanics*, John Wiley, Hoboken, N. J.
- Lu, N., and W. J. Likos (2006), Suction stress characteristic curve for unsaturated soil, *J. Geotech. Geoenviron. Eng.*, *132*(2), 131–142.
- Lu, N., B. Sener-Kaya, and J. Godt (2011), Direction of unsaturated flow in a homogeneous and isotropic hillslope, *Water Resour. Res.*, *47*, W02519, doi:10.1029/2010WR010003.
- Meisina, C., and S. Scarabelli (2007), A comparative analysis of terrain stability models for predicting shallow landslides in colluvial soils, *Geomorphology*, *87*(3), 207–223.
- Mirus, B., B. Ebel, K. Loague, and B. Wemple (2007), Simulated effect of a forest road on near-surface hydrologic response: Redux, *Earth Surf. Processes Landforms*, *32*(1), 126–142.
- Montrasio, L., and R. Valentino (2008), A model for triggering mechanisms of shallow landslides, *Nat. Hazards Earth Syst. Sci.*, *8*(5), 1149–1159.
- Morgestern, N. R., and V. E. Price (1965), The analysis of stability of general slip circles, *Geotechnique*, *1*(15), 79–93.
- Pack, R. T., D. G. Tarboton, and C. N. Goodwin (Eds.) (1998), *The SINMAP Approach to Terrain Stability Mapping*, vol. 2, 8th Congress Assoc. of Eng. Geol., British Columbia, Canada.
- Parlange, J. (1972), Theory of water movement in soil: 8. One dimensional infiltration with constant flux at the surface, *Soil Sci.*, *114*, 1–4.
- Philip, J. R. (1991a), Hillslope infiltration: Divergent and convergent slopes, *Water Resour. Res.*, *27*(6), 1035–1040.
- Philip, J. R. (1991b), Hillslope infiltration: Planar slopes, *Water Resour. Res.*, *27*(1), 109–117.
- Philip, J. R. (1991c), Infiltration and downslope unsaturated flows in concave and convex topographies, *Water Resour. Res.*, *27*(6), 1041–1048.
- Richards, L. A. (1931), Capillary conduction of liquids in porous mediums, *Physics*, *1*, 318–333.
- Rigon, R., G. Bertoldi, and T. M. Over (2006), Geotop: A distributed hydrological model with coupled water and energy budgets, *J. Hydrometeorol.*, *7*(3), 371–388.
- Rubin, J., and R. Steinhardt (1963), Soil water relations during rain infiltration: 1. Theory, *Soil Sci. Soc. Am. Proc.*, *27*, 246–251.
- Shao, W., T. A. Bogaard, M. Bakker, and R. Greco (2015), Quantification of the influence of preferential flow on slope stability using a numerical modelling approach, *Hydrol. Earth Syst. Sci.*, *19*(5), 2197–2212.
- Simoni, S. (2007), A comprehensive approach to landslide triggering, PhD thesis, Doctoral Stud. in Environ. Eng., Trent Univ., Trento, Italy.
- Simoni, S., F. Zanotti, G. Bertoldi, and R. Rigon (2008), Modelling the probability of occurrence of shallow landslides and channelized debris flows using geotop-fs, *Hydrol. Processes*, *22*(4), 532–545.
- Skempton, A. W., ZL. Bjerrum, A. Casagrande, and R. B. Peck (1960), Chapter: Significance of Terzaghi's concept of effective stress, in *From Theory to Practice in Soil Mechanics*, John Wiley.
- Srivastava, R., and T. C. J. Yeh (1991), Analytical solutions for one-dimensional, transient infiltration toward the water table in homogeneous and layered soils, *Water Resour. Res.*, *27*(5), 753–762.
- Taylor, D. W. (1948), *Fundamentals of Soil Mechanics*, John Wiley and Sons, N. Y.

- Terzaghi, K. (1943), *Theoretical Soil Mechanics*, John Wiley and Sons, N. Y.
- Tsai, T., and J. Yang (2006), Modeling of rainfall-triggered shallow landslide, *Environ. Geol.*, *50*(4), 525–534.
- Vanapalli, S. K., D. G. Fredlund, D. E. Pufahl, and A. W. Clifton (1996), Model for the prediction of shear strength with respect to soil suction, *Can. Geotech. J.*, *33*(3), 379–392.
- van Genuchten, M. Th. (1980), A closed-form equation for predicting the hydraulic conductivity of unsaturated soils, *Soil Sci. Soc. Am. J.*, *44*, 892–898.
- Wu, W., and R. Sidle (1995), A distributed slope stability model for steep forested basin, *Water Resour. Res.*, *31*(8), 2097–2110.
- Yeh, H.-F., and C.-H. Lee (2013), Soil water balance model for precipitation-induced shallow landslides, *Environ. Earth Sci.*, *70*(6), 2691–2701.